GNSS Reflectometry Correlation with Camera Images for Surface Type Determination

Seebany Datta-Barua, Roohollah Parvizi, *Illinois Institute of Technology*
Alison Banwell, *University of Colorado Boulder*
Shahrukh Khan, *Illinois Institute of Technology*

BIOGRAPHY

Seebany Datta-Barua is a Professor of Mechanical and Aerospace Engineering at Illinois Institute of Technology. She received a Ph.D. (2008) in aeronautics and astronautics from Stanford University. Dr. Datta-Barua researches the use of GNSS for remote sensing. She was the recipient of the 2019 ION Per Enge Early Achievement Award.

Roohollah Parvizi is a Positioning Algorithm Engineer at Hemisphere GNSS. He received a Ph.D (2020) in mechanical and aerospace engineering from Illinois Institute of Technology. His current work is on detecting scintillation for real-time kinematic (RTK) positioning.

Alison Banwell is a Research Scientist II at the Cooperative Institute for Research in Environmental Sciences (CIRES) at the University of Colorado Boulder. She received a Ph.D. (2013) in Glaciology from the University of Cambridge, UK. Her research focuses on understanding changes in Antarctic and Greenland ice-sheet and ice-shelf melt, hydrology, and dynamics.

Shahrukh Khan is a Systems and requirements engineer at Brose. He is working on development of automotive technologies. Shahrukh has a master's degree (2020) in mechanical and aerospace engineering from Illinois Institute of Technology with a thesis on camera-lidar sensor fusion, and a bachelor's degree in mechanical engineering from Air University Islamabad.

ABSTRACT

We present estimates and uncertainties of surface reflectivity (SR) at L-band for a lake surface of mixed ice and water based on GNSS signals reflected from the surface with a dedicated downward-pointing GNSS antenna. The surface reflectivity, assumed to be from the first Fresnel zone of the L1 signal, is compared to two cameras' images of the surface mapped to their location on the surface using lidar range measurements. The mean red value (MRV) of camera pixels within the Fresnel zone is used as a truth reference to distinguish surface ice from surface water. Three GPS satellites' reflectivity of the L1 signal is examined from data collected on 14 Feb 2020 for two 20-minute segments of data collection. A correlation between SR and MRV is hypothesized, and the SR from PRN 26 is moderately positively correlated with the MRV. However, the data from PRN 16 are moderately negatively correlated, and from PRN 27 are uncorrelated although the sample size for this PRN is too small to be conclusive. Inspection of the lidar point cloud projected onto the camera image plane indicates a possible misalignment of the camera images being used with the estimated Fresnel zone position.

I. INTRODUCTION

Weather events in 2023 to date have brought possible effects of climate change to the forefront of public consciousness. To judge from news headlines, they seemed to be more frequent and more widespread. While weather differs from climate, a perceived acceleration may not be simply imaginary. Recent evidence by Nisbet et al. (2023), reprinted in Fig. 1 shows that atmospheric methane has recently been accelerating at a rate comparable to interglacial "termination" events that have happened in the past approximately every 100,000 years. While many extreme weather events in 2023 to date have happened in populated mid-latitudes, of the various extreme events, melt of the polar caps is one considered widely impactful both to society and with regard to climate feedbacks.

Monitoring the cryosphere is an important capability for understanding climate change and its impacts. Satellite-based imaging systems can provide coverage but revisit intervals to a given site if days, may be too long given the rapid pace of change in Earth's frozen surfaces. Optical imaging from space is subject to cloud cover, from air to weather conditions, and from the ground to precipitation on the lens or snow accumulation blocking the field of view. GNSS reflectometry (GNSS-R), the measurement of the reflected GNSS signal, provides an alternate method with potentially higher spatial and temporal resolution. Researchers have shown that GNSS can be used interferometrically (GNSS-IR), with a single upward-facing antenna, to measure snow depth and accumulation (Larson, 2019). The GNSS-IR technique can show seasonal variation occurring over weeks or months.

In the past several years we have used GNSS-R in a different mode – with a single antenna pointing downward to capture only

 https://doi.org/10.33012/2023.19456

the reflected signal – in order to collect GPS signals reflected from a lake surface in winter. Due to the ability of wind to cause waves on a water surface that would not be possible on a frozen ice surface, it is expected that the surface reflectivity (SR) will be higher for ice than for water. In previous work, we have estimated the surface reflectivity based on the SNR of the reflected GPS L1 signal, and shown it to be correlated with the mean red value of optical images of the scattering surface. For visible light, the "red" value of the RGB triplet for a pixel is high for ice (producing a white pixel), and is low for water (which has green and blue but much less red) (Parvizi et al., in press). In this work, we test the replicability of that finding with other data sets that were previously obtained in 2020 but not yet analyzed. We also develop a method for quantifying the uncertainty on our GNSS-R-based estimates of the surface reflectivity.

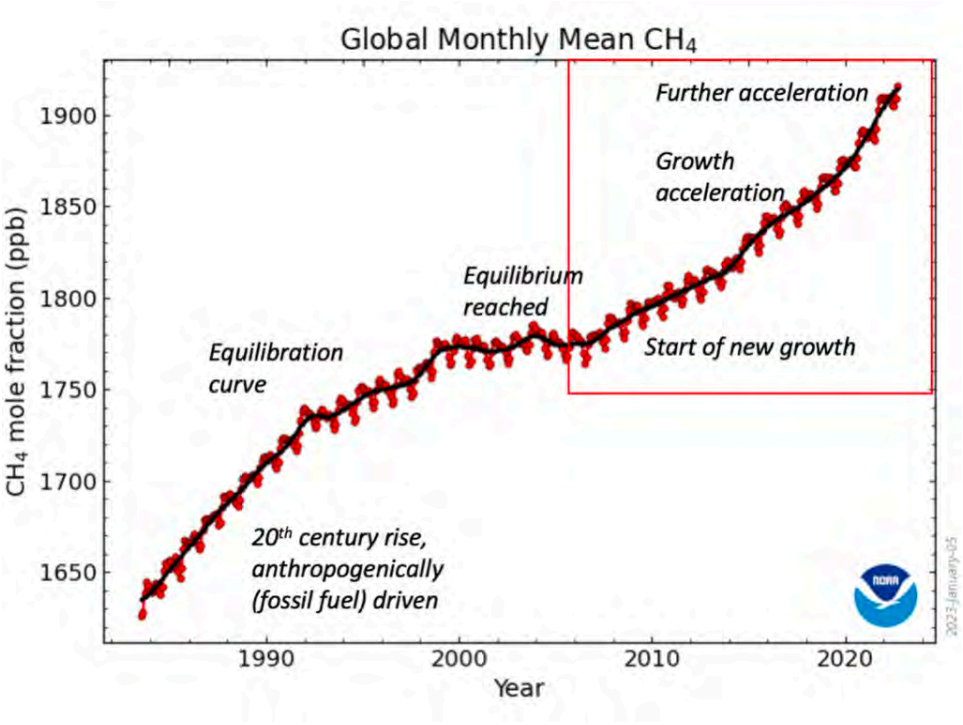

Figure 1: Figure reprinted from Nisbet et al. (2023): Global monthly mean of atmospheric methane, NOAA network. The curve decelerates to a source-sink equilibrium from the 1980s to early 2000s. Then growth began again in 2007, with an increasing rate (acceleration of growth) in 2013, and further acceleration in 2020.

II. METHOD

Our method repeats the methodology described in Parvizi et al. (in press). To summarize the procedure, we will collect GNSS reflected signals from a mixed surface at the same time that we use cameras and lidars as truth reference for the surface type. We will use the GNSS-R signals to compute the signal-to-noise ratio as:

$$SNR = \frac{P_{max} - P_{noise}}{P_{noise}} \tag{1}$$

The surface reflectivity is related to the SNR as:

$$SR \sim SNR - P^t - G^t - G^r - 20\log(\lambda) + 20\log(R_{ts} + R_{rs}) + 20\log(4\pi) \tag{2}$$

Meanwhile, we use the lidar to sense the surface height from the sensor system (the lidar reflects from ice but not water). We use this surface to backward project the camera images from the 2D camera image plane back to 3D space, interpolating to the lidar points where the lidar and camera fields-of-view overlap. We will compute the positions of each PRN's specular point and first Fresnel zone. From the camera image of the surface, we find the pixels that lie within the Fresnel zone and compute their mean red value MRV. The MRV will be high for ice, which tends to be white corresponding to an RGB triplet of (1,1,1), and low for liquid water which will be more blue-green corresponding to (0,1,1).

In this work, we now estimate errors on the SR by taking the sample standard deviation in SNR over each minute. The estimated uncertainties are then converted to dB for calculating the surface reflectivity SR according to Eq. (2).

1. Fieldwork

Data were collected in the field on 14 Feb 2020, which we refer to as "Test 10." The location of the system setup is shown in the Google Map in Fig. 2a. The GNSS antennas are mounted on a boom supported by a tripod placed at the edge of the lake with the boom oriented along $\hat{b}$ over the water. Below the antenna boom, the lidar and cameras are mounted on a shorter platform extending in the direction of $\hat{b}$ also. Figure 2b shows a photo of the tripod-mounted sensors. These are connected to a power supply and electronics, including two universal software radio peripherals (USRPs) and network switches, inside an electronics box. The data from the network switches (one for the USRPs and the other for the lidar and cameras) are fed to the laptop with external storage devices (shown in the foreground). A complete system connection schematic is provided in Parvizi et al. (in press).

For Test 10 the lake surface was a mixture of ice and water. Table 1 lists the system configuration parameters for the fieldwork. The angles are defined in CAD diagrams of the physical dimensions of the tripod in Parvizi et al. (in press). While the camera 2 relative heading μ_2 and elevation ψ_2 are nominally -25° and -36°, respectively, analysis by Khan (2020) indicated a need for manual adjustment to -24° and -39°, since the process of transporting and setting up the sensor system can loosen some of the camera hinge joints.

Table 1: Lake Michigan data collection campaign information for Test 10

Date	Fri, 14 Feb 2020
Latitude	41.83835°
Longitude	-87.60615°
Altitude	172 m
Sampling rate	5 MHz
direct USRP inline gain	30 dB
reflected USRP inline gain	40 dB
direct USRP RF gain	31 dB
reflected USRP RF gain	31 dB
Ground plane dimension direct	19.6875" x 19.6875" x 0.04"
Ground plane dimension reflected	19.6875" x 19.6875" x 0.04"
Clock used	GPS-DO
heading angle μ of the boom with respect to north	70°
Relative heading angle μ_2 of camera 2	-24°
Relative heading angle μ_3 of camera 3	25°
Elevation angle κ of reflected antenna	-45°
Elevation angle of lidar and central camera ψ_1	-45°
Elevation angle of camera 2 ψ_2	-39°
Elevation angle of camera 3 ψ_3	-36°
Surface condition	mixed ice and water

2. Post-processing

After data are collected, they are returned to the lab. The processing follows the method of Parvizi et al. (in press), and may be summarized as follows. For each satellite the USRP data samples from the reflected antenna are used to compute the SNR using Eq. (1), once per second, with 1 ms of coherent integration, and summed incoherently for 1 s. The mean SNR over one minute is taken as the estimated value.

As in Parvizi et al. (in press), the surface reflectivity relative to the value of SR at the first minute of the data segment is used, to account for possible variations in the automatic gain control of the USRP changing between continuous data collection parts (each typically 20 minutes long). Meanwhile, we use a skyplot to target satellites in the relevant part of the sky likely to give

(a) Google Map satellite image marking Test 10 site and azimuth angle μ of instrument boom.

(b) The hardware setup at the dock for Lake Michigan Test 10. Photo credit: David J. Stuart.

Figure 2: Satellite image annotated with Test 10 location and photo of sensor system on-site.

reflections off the lake surface. We compute these satellites' positions $\vec{r}^{\,sv/R_0}$. Using the lidar point cloud to compute the lake surface height below the antenna along with the satellite azimuth and elevation, we compute the position $\vec{r}^{\,sp/R_0}$ of the specular point (sp) relative to the reflected antenna (R_0). These position vectors are used to compute path loss distances R_{ts}, R_{rs}, and the gain G^r in the direction of the specular point from the reflected antenna. A table of the gain G_r as a function of the antenna zenith angle is given in Parvizi et al. (in press). Combining these values according to Eq. (2) yields an estimate of the surface reflectivity SR.

Since the SNR is computed once per minute, the lidar and camera data are downsampled to one-minute cadence also. For computing the mean red value, the lidar point cloud is cropped to consider only the points sampling the lake surface and then projected onto the camera image plane. Since the lidar scans over a limited elevation range, its field-of-view (FOV) doesn't sample the entire of the FOV cameras, in particular the more distant parts of the lake. The lidar also produces no point cloud returns over water. For pixels beyond the lidar sampling zone, surface heights are estimated with a pseudo-point cloud extrapolated from the ranges of the true point cloud points, by fitting a plane to them. These distances are then interpolated to every camera pixel and the camera pixels are projected from the 2D image plane onto a 3D region to give $\vec{r}^{\,p/R_0}$ for each pixel p in coordinates east-north-up (ENU) from the reflected antenna R_0.

Just as the specular point positions $\vec{r}^{\,sp/R_0}$ are computed, the points on the perimeter of the first Fresnel zone (FZ) are computed

first as parameters of an ellipse about the specular point and then transformed to $\vec{r}^{FZ/R_0}$ in ENU coordinates. The position of the camera pixels lying within the polygon subtended by the Fresnel zone points are selected for their RGB values. From these the MRV is computed.

Before comparing ΔSR to MRV, we ensure that 1) the satellite is below the reflection antenna's body horizon by checking that $\vec{r}^{sv/R_0}$ has an elevation angle greater than 90° relative to the antenna zenith; and 2) the full FZ lies within the cameras' FOV by checking that the area of the convex hull of the pixels that lie within the FZ are at least 99% of the area of the convex hull of the set of point $\vec{r}^{FZ/R_0}$. If these two criteria are met, then we compare the relative surface reflectivity to the mean red value, for that satellite for that time.

III. RESULTS

Figure 3 shows sky plots of the GPS satellite positions in the sky for the data sets whose results are shown. Figure 3a shows the start time of Test 10, Part 1, and Fig. 3b shows the start time of Part 3. Because the lake surface is to the east of the sensor system, satellites to the east will have specular points reflect on the lake surface. In addition, we require that satellites in the sky be below the reflected antenna's body-frame horizon to reduce direct path power. Since the downward antenna has an elevation angle of 45°, this corresponds to PRNs in the sky that are at an elevation above about 45°. These criteria indicate that PRN 16 is in the useful region for the duration, PRN 26 is in the acceptable region for Part 1, and PRN 27 may be rising into the usable region toward the end of the Part 3 time. PRNs 16, 26, and 27 will be the satellites on which the results will focus.

Figure 4 show multi-camera images taken at (left) 18:28 UT and (right) 19:00 UT, projected onto a map east and north of the sensor system, which is located at the green 'x.' The specular reflection points for several PRNs are marked with orange circles, and the first Fresnel zone for each is shaded transparent red. The surface has plates of ice to the southeast of the sensor and only water to the northeast. The specular points and Fresnel zones of PRNs 16, 26, and 27 are to the east of the sensor system, as expected. From Part 1 (Fig. 4 left), it is clear that the Fresnel zones of PRN 16 and PRN 27 are not entirely within the cameras' fields of view. PRN 16 is so high in the sky that the cameras, which are tilted at an elevation angle of -36° do not view its entire FZ. For this reason PRN 26 is the only satellite whose SNR will be used to calculated the SR of the surface from Part 1 of the data set.

PRN 26 begins to the northeast, sampling some thin ice with water underneath. It moves slightly further to the northeast as time progresses. By the start of Part 3 though, it is below 45 deg elevation, which means that the satellite itself might be above the reflection antenna's horizon, so those times end up being excluded from consideration. As a result, the SR from PRN 26 will be compared to the MRV for Part 1 only.

At 19:00 UT, the Fresnel zone of PRN 27 is almost entirely within the FOV of camera 3. For some of the Part 3 data segment, the entire FZ will be within the FOV of the camera, and for those times the MRV will be usable for comparison. At 19:00 UT the FZ of PRN 27 is reflecting primarily off ice but there is a break in the ice in the northern part of the FZ ellipse.

Figure 5 compares the relative surface reflectivity ΔSR and the mean red value MRV, which meet the comparison criteria during Part 1 of the data set only. The upper plot shows each as a function of time, with ΔSR plotted in blue with sample standard deviations taken over each minute, and the dimensionless MRV in red. The error bars are not symmetric about the estimated value in general since the scale is logarithmic. The relative SR spans about 0.6 dB, and the MRV spans about 0.04 in red value. The lower subfigure is a scatter plot of the MRV versus ΔSR. The correlation coefficient between these values for PRN 26 is $\rho = 0.53$, or moderate correlation.

A comparison of the relative surface reflectivity estimated from the SNR of PRN 16 to the mean red value over its Fresnel zone is shown in Fig. 6. In the upper subplot, ΔSR is shown in blue with error bars and MRV plotted in red. The relative SR plot scale spans 3 dB (much wider than that of Fig. 5), while the MRV still spans 0.04 in red value variation. Here the MRV shows an increasing trend, meaning a shift from more to less surface ice. However, the relative surface reflectivity shows no such trend. Note that the dB span is wider in this subplot than in Fig. 5, which means that at some times the error bars may as much as 1 dB. In the lower scatter plot a moderate negative correlation is visible; the correlation coefficient is $\rho = -0.58$.

The Fresnel zone of PRN 27 has moved into the cameras' FOV by the later times in Part 3 of the data set. For this reason its surface reflectivity and mean red values are selected for comparison from 19:11-19:19 UT. Figure 7 shows (a) their time series and (b) a scatter plot of their correlation for the data during this time interval. Uncertainties on the SR are about 0.2 dB. The MRV decreases from 0.47 to 0.45 over the last five minutes. There is almost no correlation, with $\rho = -0.18$. However, in this data set there are only 8 points.

The correlation plots from the three satellites analyzed so far for this test appear to be inconclusive regarding the degree of correlation between SR and MRV. While we may consider PRN 27 as having too few comparable measurements to be significant, it is interesting to note that the part of the surface spanned by the Fresnel zone of PRN 26 in Part 1 is sampled by the Fresnel zone of PRN 16 later in time, during Part 3. And yet they produce opposite senses of correlation.

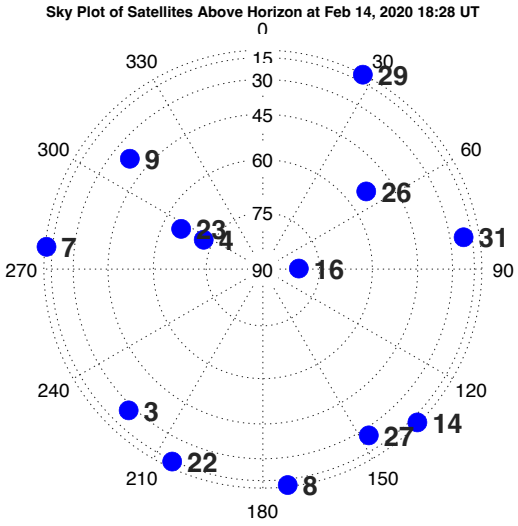

(a) Sky plot at 18:28 UT on 14 Feb 2020, corresponding to the start of Test 10, part 1.

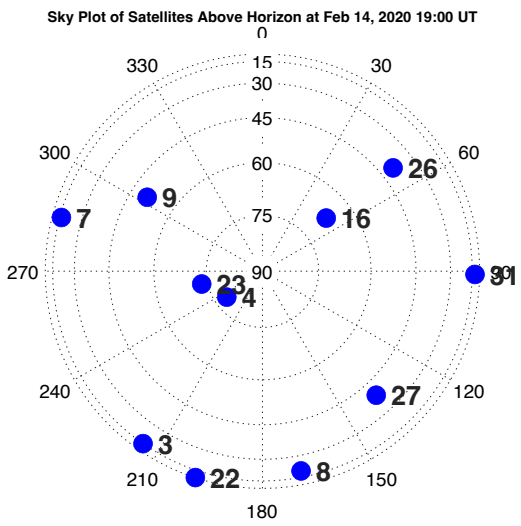

(b) Sky plot at 19:00 UT on 14 Feb 2020, corresponding to the start of Test 10, part 3.

Figure 3: Sky plots for 14 February 2020 at (a) 12:28 central time (CT) at the start of Test 10, Part 1, and (b) 13:00 CT at the start of Test 10 Part 3.

One possible cause of this poor correlation may be due to errors in sensor alignment for the purposes of mapping the camera images on the surface, which impacts the pixels identified as lying within the Fresnel zone. Figure 8 shows the lidar point cloud scans as colored dots overlaid on the 2D camera image from camera 2 at 19:00 UT at the start of Part 3. The lidar point cloud is projected onto the image plane, measured in pixels, and each point's color corresponds to the lidar range. This image is produced as an intermediate step in the projection of a camera image onto the 3D ENU coordinates. The lidar returns exist when there is solid ice but do not return reflections off water. As a result we expect the lidar point cloud to lie on regions of solid ice. One such block of ice is centered at about pixel $(u, v) = (700, 1000)$. Note that the block of ice which is whiter is approximately oval shaped. There are lidar scan returns that suggest a similar oval shape, but they are offset from the white ice region by about $dv = 100$ pixels. While some recognition of this measurement error was taken into account in the parameters in Table 1, it is possible that errors in the angular measurement of the camera's orientation (which is adjustable) relative to the lidar, contributes to some of the lack of correlation. This would affect both the results for PRNs 26 and 16. The alignment of camera 2 would not affect the results of PRN 27, which is primarily imaged by camera 3, but a similar such problem may lie there. Future study should consider quantifying the lidar-camera mapping uncertainty and the impact it has on the MRV calculation.

Another factor based on the uncertainties on the SR calculation for PRN 16 in Fig. 6, is that longer coherent integration times might be useful in producing better estimates of the surface reflectivity. Nevertheless there is an increase in the variation in SNR, leading to a 1 dB uncertainty, even though the same 1 ms coherent integration time is used in both cases. It is possible this increase in uncertainty indicates more surface motion as the surface ice melts and breaks up during the day.

IV. SUMMARY AND FUTURE WORK

In this work, we compared the relative surface reflectivity computed from GNSS reflected from a lake surface with a heterogeneous mix of ice and water, and compared them to images of mixed ice and water. This work repeats the methodology of Parvizi et al. (in press) but includes estimates of the uncertainty on the SR. Preliminary results are inconclusive because one PRN comparison shows positive correlation and another sampling a similar part of the surface at a later time, shows negative correlation. This disagrees with the finding by Parvizi et al. (in press) of moderate correlation between SR and MRV. We find that uncertainty in the mapping alignment of lidar, camera, and Fresnel zone may play a role, and that the negatively correlated samples had larger SR uncertainties, which may be improved by increased coherent integration. Future work will include adjusting the alignment of the lidar and camera, including uncertainties on the MRV estimate, and testing the coherent integration time for improving the uncertainty on the SNR.

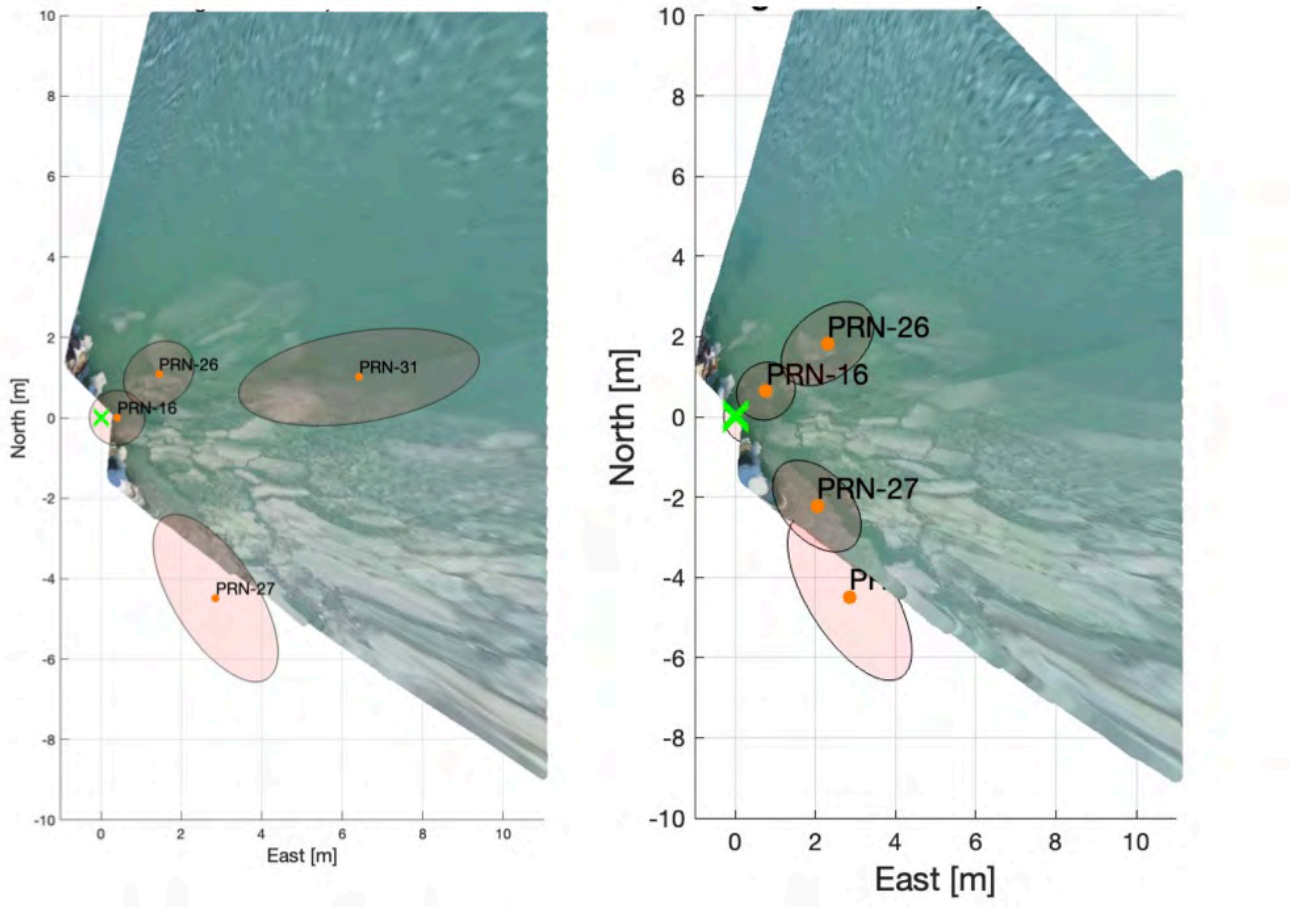

Figure 4: Fresnel Zone (FZ) mapping and camera pixel selection at (a) 18:28 UT and (b) 19:00 UT. Local time is UT minus 6 hours.

ACKNOWLEDGEMENTS

This research was supported NASA NNX15AV01G, and NSF awards 1940473 and 1940483. The authors thank the Chicago Park District for research access permits, and the students of the Space Weather lab for providing on-site help during fieldwork.

REFERENCES

Khan, S. (2020). *3D Reconstruction of Lake Surface Using Camera and Lidar Sensor Fusion*. MS thesis, Illinois Institute of Technology.

Larson, K. M. (2019). Unanticipated uses of the global positioning system. *Annual Rev. Earth and Planet. Sci.*, 47:19–40.

Nisbet, E. G., Manning, M. R., Dlugokencky, E. J., Michel, S. E., Lan, X., Röckmann, T., Denier van der Gon, H. A. C., Schmitt, J., Palmer, P. I., Dyonisius, M. N., Oh, Y., Fisher, R. E., Lowry, D., France, J. L., White, J. W. C., Brailsford, G., and Bromley, T. (2023). Atmospheric methane: Comparison between methane's record in 2006–2022 and during glacial terminations. *Global Biogeochemical Cycles*, 37(8):e2023GB007875. e2023GB007875 2023GB007875.

Parvizi, R., Datta-Barua, S., Banwell, A. F., and Khan, S. (in press). Surface reflectivity variations of GNSS signals from a mixed ice and water surface. *Navigation*.

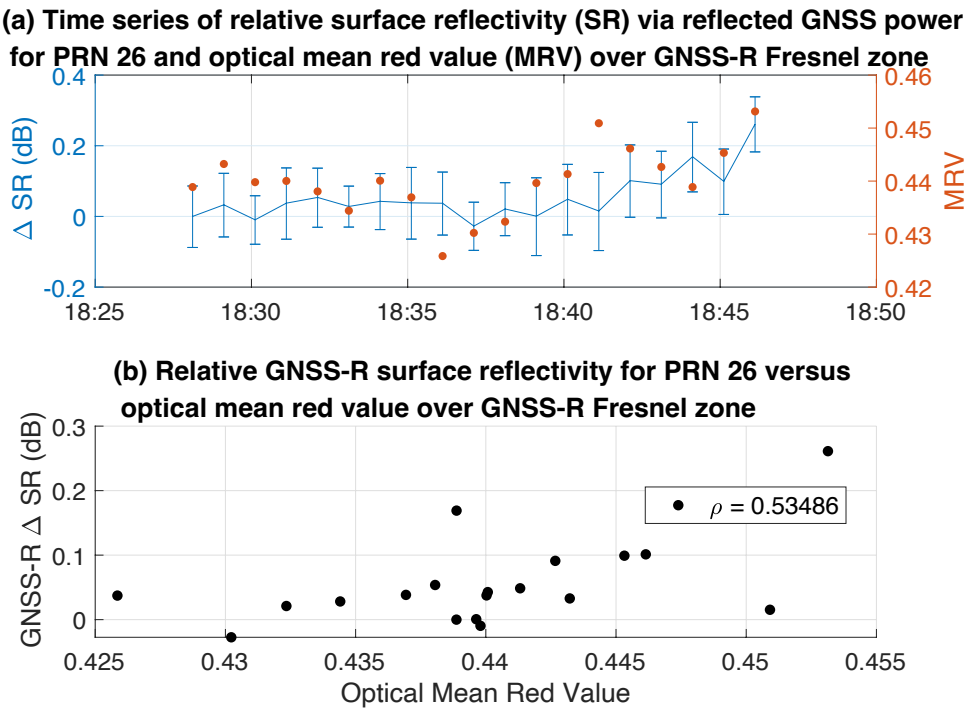

Figure 5: (a) Relative SR (blue) and MRV (red) over UT time for PRN 26 and (b) relative SR versus MRV for PRN 26

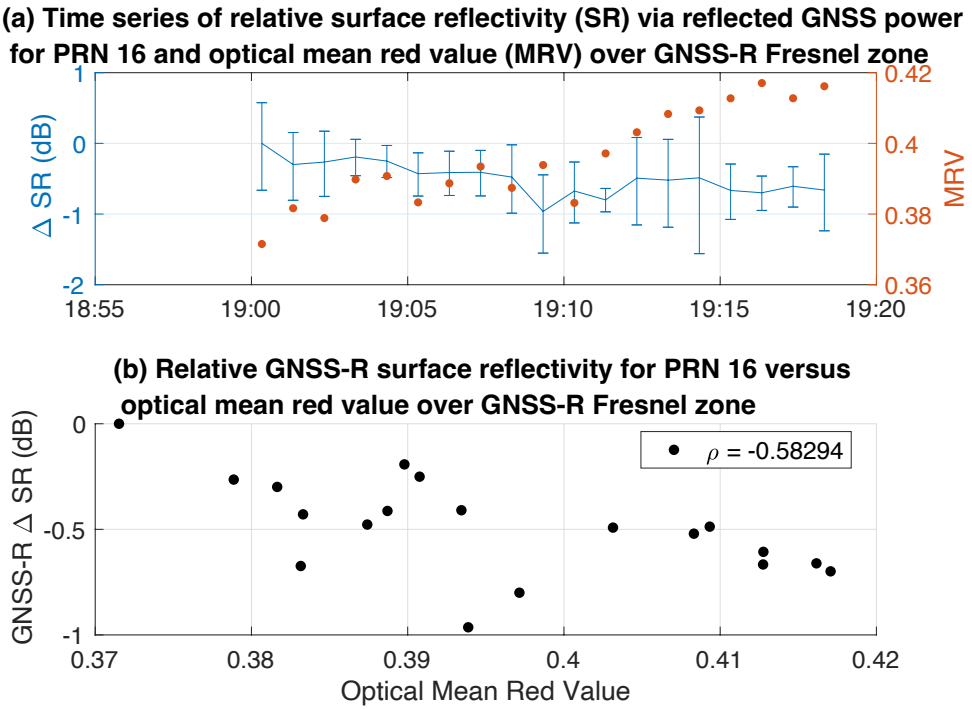

Figure 6: (a) Relative SR (blue) and MRV (red) over UT time for PRN 16 and (b) relative SR versus MRV for PRN 16

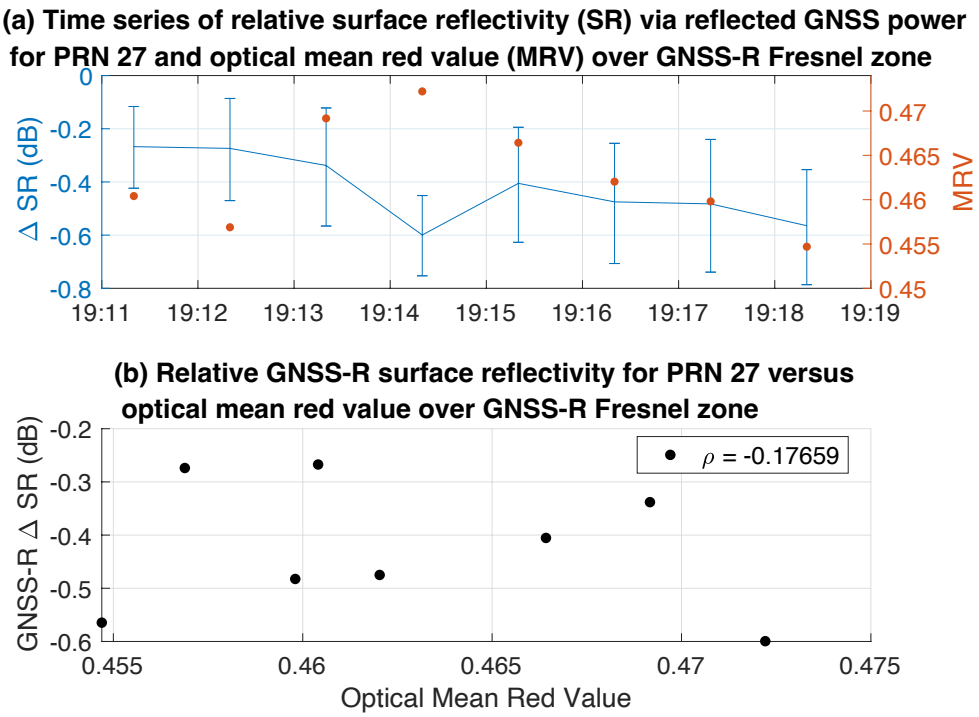

Figure 7: (a) Relative SR (blue) and MRV (red) over UT time for PRN 27 and (b) relative SR versus MRV for PRN 27

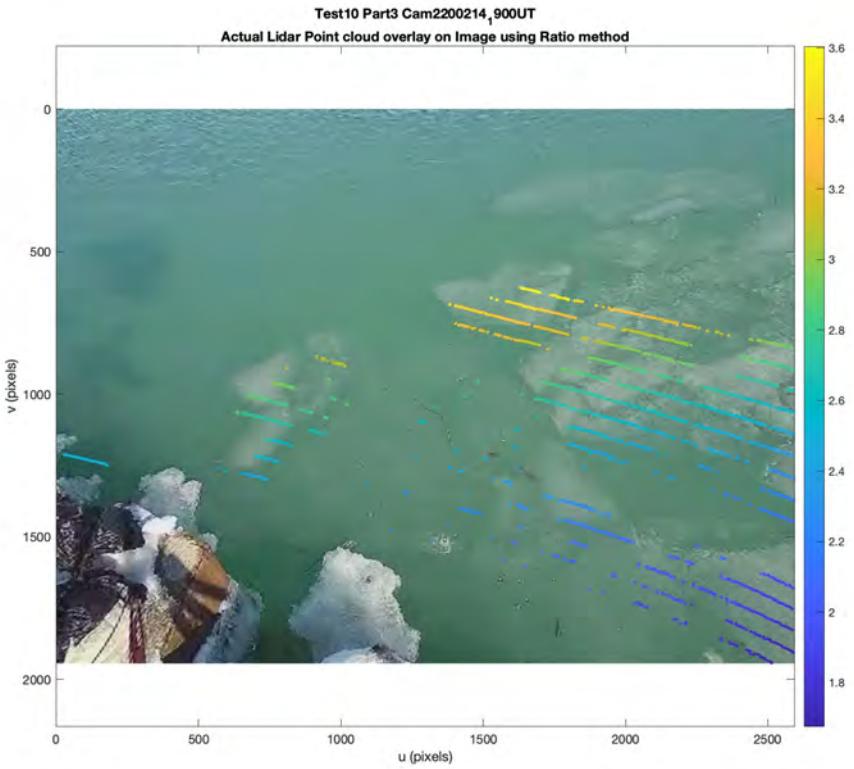

Figure 8: Projection of lidar point cloud points onto the camera image plane (u, v). Point cloud colors correspond to the lidar range measured, in meters. Each lidar scan sweeps 360° of lidar azimuth but the lidar does not reflect from the water surface.